THE JOURNAL OF PHYSICAL CHEMISTRY A

Article

Cite This: *J. Phys. Chem. A* 2019, 123, 7720−7732

pubs.acs.org/JPCA

Femtosecond Stimulated Raman Scattering from Triplet Electronic States: Experimental and Theoretical Study of Resonance Enhancements

Matthew S. Barclay, Marco Caricato,* and Christopher G. Elles*

Department of Chemistry, University of Kansas, Lawrence, Kansas 66045, United States

Supporting Information

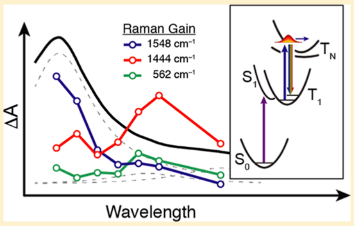

ABSTRACT: Femtosecond stimulated Raman scattering (FSRS) is a spectroscopic technique that probes the structural dynamics of molecules. The technique typically relies on an electronic resonance condition to increase signal strength or enhance species selectivity, giving a Raman enhancement that is vibrational-mode-specific and depends on the character of the resonant electronic state. The resonance condition is complicated for molecules already in an excited electronic state and also for systems where multiple electronic states are resonant or nearly resonant with the Raman excitation energy, both of which are often the case for FSRS. This paper examines the excitation wavelength dependence of the FSRS spectrum for the lowest triplet state of 2-phenylthiophene (PT). Except for an overall increase of the signal strength due to the resonance condition, the relative intensities of most Raman bands are relatively insensitive to the excitation wavelength, and the spectrum is remarkably similar to the calculated off-resonance spectrum obtained by neglecting the resonance condition. On the other hand, calculated resonance Raman spectra using a gradient approximation to simulate the resonance condition correctly predict the excitation wavelength dependence for a few modes but overestimate the relative enhancement of others. The weak wavelength dependence of the triplet spectrum of PT contrasts the case of the singlet FSRS spectrum for the same molecule. We attribute this discrepancy to a combination of homogeneous broadening, overlapping $T_N \leftarrow T_1$ transitions, and possibly vibronic coupling among states in the triplet manifold. This work highlights important limitations in using standard approaches to simulate excited-state resonance Raman spectra.

1. INTRODUCTION

Femtosecond stimulated Raman scattering (FSRS) is a time-resolved technique that provides detailed information about the structural evolution of molecules.[1−4] By monitoring changes in the vibrational spectrum following photoexcitation, the dynamics of the molecular structure and bonding is observed as the system evolves along the excited- and/or ground-state potential energy surfaces. FSRS measurements often tune the Raman excitation wavelength to match an electronic transition of a target molecule in order to give a resonance enhancement of the transient Raman signal. Resonance with a specific electronic state increases the Raman transition strength of some modes by up to several orders of magnitude, depending on the character of the resonant electronic state.[5−7] Thus, tuning to a particular resonance in the transient absorption spectrum allows for the selective measurement of Raman transitions from a particular species along the reaction path while also significantly improving the signal-to-noise ratio.[8−15]

However, mode-specific resonance enhancements complicate the interpretation of FSRS spectra, particularly the assignment of the observed Raman bands to specific vibrational modes of the molecule in an excited state.[5,6,16] Although some assignments are possible based on simple chemical intuition and comparison with vibrational frequencies from the ground electronic state, calculated frequencies and intensities are important for making accurate assignments in the excited state, particularly in regions of the spectrum with a high density of vibrational states. The excited-state vibrational frequencies are relatively easy to compute, but the Raman intensities are more challenging because they require the evaluation of changes in the excited-state polarizability tensor along each of the vibrational coordinates.[17−22]

Using a series of conjugated thiophene derivatives for benchmark comparison, we showed that it is possible to assign resonance-enhanced FSRS bands for a series of structurally similar molecules by calculating the off-resonant excited-state Raman spectra and carefully considering which vibrational modes are most likely to be enhanced by the electronic resonance.[19] Vibrations with the strongest scattering signals have significant nuclear displacement along the potential energy surface of the resonant higher-lying excited state relative to the initial state upon $S_N \leftarrow S_1$ or $T_N \leftarrow T_1$ excitation with the Raman pump pulse. In a second contribution, we examined the resonance condition explicitly using a gradient approximation of the time-dependent resonance Raman (TD-RR) theory to simulate the experimental FSRS spectrum of the S_1 state of 2,5-diphenylthiophene (DPT).[23] The simulated spectrum qualitatively reproduced the mode-specific resonance

Received: June 21, 2019
Revised: August 16, 2019
Published: August 17, 2019

enhancements by matching the gradients in a specific excited state (S_N) to the assigned vibrations of S_1.

In contrast with the S_1 spectra, where the resonance enhancement is strongly mode-dependent, the calculated off-resonance Raman spectra of the triplet states are in close agreement with the experimental FSRS spectra for the T_1 states of DPT and other aryl thiophenes in our benchmark series.[19] A similarly weak wavelength dependence of the resonance Raman spectrum has been observed for triplet states of other conjugated organic systems,[24−26] suggesting that triplet states may be less sensitive to mode-dependent resonance enhancement compared with the singlet states of the same molecules. In this manuscript, we explore the weak wavelength dependence of the triplet Raman spectrum of the model compound 2-phenylthiophene (PT) in more detail. Comparing experimental FSRS spectra at different Raman excitation energies with theoretical simulations of the on- and off- resonance spectra, we determine that the weaker mode dependence of the T_1 Raman intensities compared with S_1 is a result of contributions from overlapping electronic transitions and increased homogeneous broadening of resonant T_N states, possibly due to nonadiabatic coupling within the triplet manifold.

This paper is organized as follows. We briefly recount the relevant aspects of the time-dependent theory for resonance Raman scattering in Section 2 and then summarize our experimental and theoretical approaches in Section 3. We compare the experimental and calculated electronic absorption spectra for the triplet state of PT in Section 4.1 and assign the vibrational bands of the FSRS spectrum with off-resonant calculations of the T_1 Raman spectrum in Section 4.2. In Sections 4.3 and 4.4, we examine the excitation wavelength dependence of the T_1 FSRS spectrum and then compare it to simulations of resonance Raman spectra obtained using two methods: (1) an extrapolation of harmonic potentials and (2) the gradient approximation of TD-RR theory. Finally, we discuss the results in Section 5 and summarize our main conclusions in Section 6.

2. THEORY

In order to motivate the different computational approaches used in the following sections, we begin with a brief summary of Raman scattering theory. More extensive descriptions of Raman and resonance Raman (RR) scattering are available in the literature.[7,16−18,27−31]

The intensity of a Raman transition from an initial vibrational state $|\nu_i\rangle$ to a final state $|\nu_f\rangle$ is proportional to the square of the transition polarizability tensor,

$$I \propto \omega_p(\omega_p - \omega_{fi})^3 \, |\alpha_{fi}|^2 \tag{1}$$

where ω_p is the incident photon frequency and ω_{fi} is the frequency of the vibrational transition. As introduced by Kramers, Heisenberg, and Dirac,[32] and also in the Placzek formulation of the second-order time-dependent perturbation theory,[33] the generic expression for the transition polarizability between any two initial and final states $|i\rangle$ and $|f\rangle$ can be written as a sum over states,

$$\alpha_{fi} = \frac{1}{\hbar}\sum_n \left(\frac{\langle f|\hat{\mu}|n\rangle\langle n|\hat{\mu}|i\rangle}{\omega_{ni} - \omega_p - i\Gamma_n} + \frac{\langle f|\hat{\mu}|n\rangle\langle n|\hat{\mu}|i\rangle}{\omega_{nf} + \omega_p + i\Gamma_n} \right) \tag{2}$$

where $\{|n\rangle\}$ are all possible intermediate vibronic states, Γ_n are phenomenological broadening terms related to the dephasing of each intermediate state, $\hat{\mu}$ is the electric dipole operator, and ω_{ni} and ω_{nf} are the transition frequencies.

Due to the difficulty of evaluating the full sum-over-states expression in eq 2, the transition polarizability can instead be recast in terms of a Taylor series expansion of the full electronic polarizability (α) with respect to the mass-weighted displacement of each vibrational coordinate q_k,

$$\alpha_{fi} = \alpha_0\langle \nu_f|\nu_i\rangle + \sum_k \left(\frac{\partial \alpha}{\partial q_k}\right)_0 \langle \nu_f|q_k|\nu_i\rangle + ... \tag{3}$$

where the subscript 0 indicates values at zero displacement of a vibration. Neglecting higher-order terms in the expansion and assuming harmonic normal modes and an off-resonance electronic condition ($\omega_p = 0$), the transition polarizability for the fundamental of each vibrational mode k is proportional to the electronic polarizability derivative with respect to q_k,[17,18]

$$\alpha_{fi}^k \propto \sqrt{\frac{\hbar}{2\omega_k}}\left(\frac{\partial \alpha}{\partial q_k}\right)_0 \tag{4}$$

where ω_k is the vibrational frequency of the mode.

The Raman activity increases substantially when the incident pump field is at or near resonance with an electronic transition, in which case the transition polarizability is no longer simply described by eq 4. The enhancement of the Raman signal is a result of the small denominator in the first term of eq 2 as ω_p approaches ω_{ni}. Thus, the expression for the transition polarizability in eq 2 reduces to a sum over intermediate vibrational states $|\nu_n\rangle$, assuming that the Born−Oppenheimer approximation holds and in the limit of weak vibronic coupling.[5,17,27,34] For resonance with a single electronic state, the sum includes only vibrational levels of the resonant electronic state $|N\rangle$. The second term in eq 2 is negligible under resonance or near-resonance conditions.[17]

In the time-dependent formalism for resonance Raman scattering, the denominator in the first term of eq 2 is converted from the frequency domain to the time domain through a Fourier transform,[7,17,28,31]

$$\alpha_{fi} \approx \frac{i}{\hbar}\sum_{\nu_n}\int_0^\infty \langle \nu_f|\mu_{IN}|\nu_n\rangle\langle \nu_n|\mu_{NI}|\nu_i\rangle e^{-i(\omega_n - \omega_i - \omega_p - i\Gamma_n)t}\,dt \tag{5}$$

where $\langle \nu_f|$ and $|\nu_i\rangle$ are both within the initial electronic state $|I\rangle$, μ_{NI} is the electronic transition dipole between the initial and intermediate electronic states, and ω_n and ω_i are the energies of the intermediate and initial vibronic states, respectively. The sum over states $|\nu_n\rangle$ gives a time-dependent wavepacket that evolves according to $\hat{H}_N$, the Hamiltonian describing nuclear motion in the intermediate electronic state $|N\rangle$.[5,7,17,35] Thus, we recast eq 5 as the time-integrated overlap of the wavepacket in the resonant state $|\nu_i(t)\rangle = e^{-i\hat{H}_N t/\hbar}|\nu_i\rangle$ with the vibrational wave function of the final state $\langle \nu_f|$.[23]

$$\alpha_{fi} \approx \frac{i}{\hbar}\int_0^\infty |\mu_{NI}|^2 \langle \nu_f|e^{-i\hat{H}_N t/\hbar}|\nu_i\rangle e^{i(\omega_i + \omega_p + i\Gamma_n)t}\,dt \tag{6}$$

An implicit assumption in eq 6 is that the electronic transition dipole follows the Condon approximation, which gives only the A term in the Albrecht description of Raman scattering.[17,27,36] The other Albrecht scattering terms (B, C, and D) are a result of Herzberg−Teller (HT) vibronic coupling between electronic states. The vibronic coupling terms arise from a perturbative expansion of the transition dipole in the nuclear coordinates of intermediate electronic state $|N\rangle$.[17,35]

$$\mu_{NI} = (\mu_{NI})_0 + \sum_j \left(\frac{\partial \mu_{NI}}{\partial q_j^{(N)}}\right)_0 q_j^{(N)} + \ldots \tag{7}$$

The derivative of the electronic transition dipole with respect to the nuclear coordinates $q_j^{(N)}$ gives the vibronic coupling of electronic states $|N\rangle$ and $|I\rangle$ with all other states $\{|M\rangle\}$ as a perturbation of the electronic Hamiltonian $\hat{H}_{\text{elec}}$.[17]

$$\left(\frac{\partial \mu_{NI}}{\partial q_j^{(N)}}\right)_0 = \frac{1}{\hbar}\left\{\sum_{M \neq I} (\mu_{NM})_0 \frac{\left\langle M \middle| \frac{\partial \hat{H}_{\text{elec}}}{\partial q_j^{(N)}} \middle| I \right\rangle}{\omega_I - \omega_M} + \sum_{M \neq N} \frac{\left\langle N \middle| \frac{\partial \hat{H}_{\text{elec}}}{\partial q_j^{(N)}} \middle| M \right\rangle}{\omega_N - \omega_M} (\mu_{MI})_0 \right\} \tag{8}$$

Substituting the expansion for μ_{NI} and truncating eq 7 at first order yields a more complete form of the transition polarizability.

$$\begin{aligned}\alpha_{\text{fi}} \approx \frac{i}{\hbar}\int_0^\infty \text{d}t\ \text{e}^{i(\omega_\text{i}+\omega_\text{p}+i\Gamma_n)t}\Bigg\{&|(\mu_{NI})_0|^2 \langle \nu_\text{f}|\text{e}^{-i\hat{H}_N t/\hbar}|\nu_\text{i}\rangle \\ &+ \sum_j (\mu_{IN})_0 \left(\frac{\partial \mu_{NI}}{\partial q_j^{(N)}}\right)_0 \langle \nu_\text{f}|\text{e}^{-i\hat{H}_N t/\hbar} q_j^{(N)}|\nu_\text{i}\rangle \\ &+ \sum_j \left(\frac{\partial \mu_{IN}}{\partial q_j^{(N)}}\right)_0 (\mu_{NI})_0 \langle \nu_\text{f}| q_j^{(N)} \text{e}^{-i\hat{H}_N t/\hbar}|\nu_\text{i}\rangle \\ &+ \sum_j \sum_l \left(\frac{\partial \mu_{IN}}{\partial q_j^{(N)}}\right)_0 \left(\frac{\partial \mu_{NI}}{\partial q_l^{(N)}}\right)_0 \langle \nu_\text{f}| q_j^{(N)} \text{e}^{-i\hat{H}_N t/\hbar} q_l^{(N)}|\nu_\text{i}\rangle \Bigg\}\end{aligned} \tag{9}$$

The first term on the right-hand side is the Albrecht A term from eq 6. Together, the second and third terms on the right-hand side are the Albrecht B and C terms, where the B term includes coupling between intermediate state $|N\rangle$ and all other electronic states and the C term includes coupling of the initial electronic state to the other electronic states. Similarly, the final term in eq 9 represents D-term scattering, which includes contributions from electronic states coupled to $|N\rangle$ and $|I\rangle$ simultaneously. Equation 8 shows that the B, C, and D terms scale with the inverse of the energy separation between the coupled electronic states and therefore are most important for states nearby in energy. It is worth noting that the polarizability derivative from eq 4 implicitly contains some degree of vibronic coupling for transitions in which only one vibrational quantum number changes.[17]

The implementation of eq 9 using computational methods has been described in detail by Baiardi et al.,[35] where the first term, containing no implicit vibronic coupling, corresponds to the Franck–Condon (FC) approximation and the B-C terms are labeled as FCHT to denote the inclusion of Herzberg–Teller coupling. This implementation uses the extrapolation of a harmonic potential expanded around the minimum-energy geometry of $|N\rangle$ in order to obtain the vibrational wave functions at the FC geometry. This approach works well for ground-state resonance Raman spectra with resonant excitation to relatively low-lying electronic states.[35,37,38] However, FSRS measurements of electronically excited systems tend to be resonant with transitions to higher-lying states where the density of states is larger and the states become more anharmonic.

An alternative to the FC and FCHT approach is the semiclassical "gradient approximation" to the TD-RR formalism,[23,28,34] where the time-dependent overlap integral $\langle \nu_\text{f}|\nu_\text{i}(t)\rangle$ is simplified by approximating the initial wave function $\langle \nu_\text{i}(t)\rangle$ with a Gaussian function at $t = 0$, which then propagates in time on the potential energy surface (PES) of the intermediate electronic state V_N according to the Hamiltonian of that state. Although the time evolution of this wavepacket depends on the topology of the PES of $|N\rangle$, the Raman intensity observed for a particular mode k depends on the time-integrated overlap of $\langle \nu_\text{i}(t)\rangle$ with the vibrational wavefunction $\langle \nu_\text{f}|$ of the final state. Thus, the time evolution of the wavepacket using classical equations of motion depends, to first order, on the gradient of the upper-state PES along each of the vibrational coordinates of the lower state $\frac{\partial V_N}{\partial q_k}$. Substituting a Gaussian wave function into eq 6 gives the simplified version of the time-dependent overlap integral,[23,28]

$$\alpha_{\text{fi}}^k \approx -\frac{i}{\hbar}|\mu_{NI}|^2 \left(\frac{\partial V_N}{\partial q_k}\right) \int_0^\infty \text{e}^{i(\omega_\text{i}+\omega_\text{p}-\omega_{NI}+i\Gamma_n)t}\,\text{e}^{-\left(\frac{\partial V_N}{\partial q_k}\right)^2 \frac{t^2}{4\omega_k}} t\ \text{d}t \tag{10}$$

where ω_{NI} is the vertical transition energy between electronic states N and I. The final expression for the resonance-enhanced Raman scattering intensity of mode k is proportional to the square of the transition polarizability term and therefore depends on the square of the gradient of the potential along q_k.[23,38]

$$I_k \propto \omega_\text{p}(\omega_\text{p} - \omega_k)^3 |\alpha_{\text{fi}}^k|^2 \approx \omega_\text{p}(\omega_\text{p} - \omega_k)^3 \frac{|\mu_{NI}|^4}{2\omega_k}\left(\frac{\partial V_N}{\partial q_k}\right)^2 \tag{11}$$

Due to computational cost, our calculations using the gradient approximation neglect vibronic coupling and therefore include only A-term scattering. However, by numerically calculating the adiabatic PES of the resonant electronic state along the nuclear displacement coordinates of T_1, the resonance Raman spectra obtained with the gradient approximation partially account for the anharmonicity of the higher-lying electronic states, unlike the FC and FCHT approaches.

In Section 4, we compare the experimental FSRS spectrum with both the off-resonance calculations and the simulated resonance Raman spectra using the FC/FCHT models (eq 9) and the gradient approximation (eq 11).

3. EXPERIMENTAL AND COMPUTATIONAL METHODS

The experimental setup for transient absorption (TA) and FSRS measurements was described previously;[23] therefore, we only summarize the main points here. We split the output of an amplified Ti:Sapphire laser (Coherent, Legend Elite HP) into three portions and use nonlinear frequency conversion to generate actinic pump, Raman pump, and Raman probe pulses. A commercial optical parametric amplifier (OPA) with two additional stages of nonlinear frequency conversion produces actinic pump pulses at 300 nm (~90 fs and ~1.0 μJ at the sample). A second commercial OPA provides tunable near-IR pulses that we subsequently pass through a 25 mm long β-barium borate (BBO) crystal to produce spectrally narrow (<0.5 nm) Raman pump pulses in the range 360−385 nm via spectral compression of the second harmonic.[39−41] We generate Raman pump pulses at 400 nm by passing a portion of the 800 nm fundamental directly through the long BBO. Passing the narrowband pulses through a 4f spectral filter eliminates asymmetry in the temporal profile and further narrows the bandwidth.[39] The resulting Raman pump pulses have ~1 ps duration, 0.3−0.7 μJ per pulse, and <30 cm^{-1} bandwidth. Using a focal diameter of ~100 μm at the sample minimizes excited-state population depletion and ensures that the resonant-FSRS signal scales linearly with pulse energy.[42] We generate fs Raman probe pulses by focusing a small portion of the 800 nm laser fundamental into a translating CaF_2 window to produce white-light continuum spanning 340−750 nm.[19,23] We use the full bandwidth of the probe pulses for TA measurements but only a narrow range of approximately 25−30 nm for FSRS. Dispersion of the uncompressed probe pulses over the narrow range of the FSRS measurement is negligible compared with the duration of the pump pulse. All three pulses overlap in the sample with parallel polarization.

After the sample, a 1/8 m imaging spectrograph with 1800 line/mm grating disperses the Raman probe pulses onto a 2068 pixel linear CCD array (Hamamatsu, S11156-2048) with instrument-limited resolution that ranges from ~45 to ~29 cm^{-1} as we tune the excitation wavelength from 360 to 400 nm. We measure the intensity of the transmitted probe light at 1 kHz, chopping the actinic pump pulses at 500 Hz and the Raman pump pulses at 250 Hz for active background subtraction. Averaging 4×10^6 laser pulses per spectrum gives a standard deviation of $<10^{-5}$ in the Raman gain signal. The baseline subtraction method is described in the Supporting Information. The sample consists of a 1.2 mM solution of 2-phenylthiophene (TCI America) in cyclohexane (spectroscopic grade, Fisher).

We calculate electronic absorption and Raman spectra using either unrestricted open-shell time-dependent density functional theory (TD-DFT) with the B3LYP or BHLYP functionals,[43,44] or the equation of motion coupled cluster theory with single and double excitations (EOM-CCSD).[45−47] B3LYP and BHLYP are global hybrid functionals with 20 and 50% Hartree−Fock (HF) exchange, respectively, that typically give good agreement with experimental ground-state Raman spectra.[48,49] In all cases, we use the aug-cc-pVDZ basis set[50] for a good compromise between accuracy and computational cost for the CCSD calculations. We calculate off-resonant T_1 Raman spectra analytically for DFT and numerically for CCSD.[51−54] We simulate the resonance Raman spectra using both the FC and FCHT approaches (B3LYP only), as well as the gradient approximation (TD-DFT and EOM-CCSD), as described above.

Due to the difficulty in optimizing the geometry of high-lying states, our resonance Raman calculations using the FC and FCHT approaches (without and with HT coupling, respectively)[35] only include the spectrum for resonance with a single upper state T_N having the strongest electronic transition strength. The contribution from T_N is determined following the adiabatic Hessian model, which includes both Duschinsky rotation and the normal mode frequency changes between states.[35] Both the FC and FCHT calculations were carried out with an incident energy equal to the adiabatic transition energy of the resonant state.

For the gradient approximation, we calculated the $T_N \leftarrow T_1$ transition moments for states up to $N = 20$ with either TD-DFT or EOM-CCSD. The gradients of the T_N potential energy surfaces were determined numerically by fitting a second-order polynomial to three points along each of the T_1 normal mode coordinates, including the optimized geometry and $\pm 7.408 \times 10^{-4}$ times the normalized displacement. The magnitude of the displacement was optimized in previous work to minimize the errors in calculated Raman activities.[19] All calculations were performed using a development version of the GAUSSIAN software package,[55] and all simulated Raman spectra include 25 cm^{-1} Gaussian broadening.

4. RESULTS AND ANALYSIS

4.1. Excited-State Absorption Spectroscopy. The evolution of the transient absorption (TA) spectrum of PT is displayed in Figure 1. After $S_1 \leftarrow S_0$ excitation at 300 nm, the

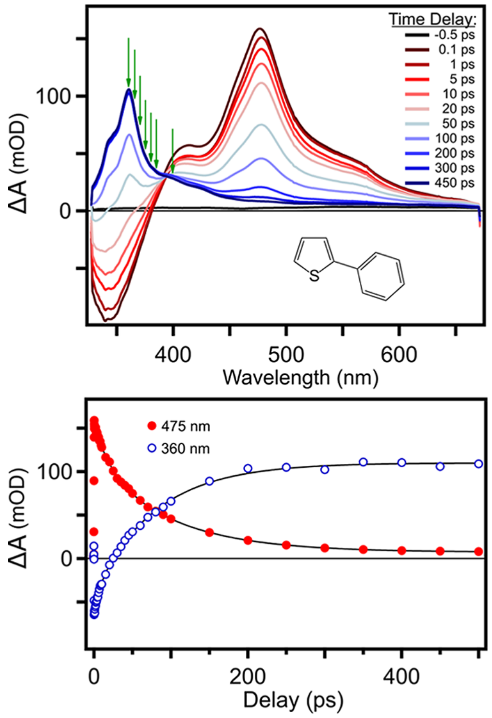

Figure 1. Evolution of the transient electronic absorption spectrum of PT following 300 nm excitation. Green arrows in the top panel indicate Raman excitation wavelengths for FSRS measurements (360−400 nm) at 408 ps delay. The lower panel shows the kinetics at 475 and 360 nm to illustrate the simultaneous decay of S_1 and rise of T_1.

TA spectrum has a strong excited-state absorption band at 475 nm and a stimulated emission band at 340 nm. The 475 nm band is attributed to absorption from the S_1 state, and narrows within the first ~10 ps due to structural relaxation and vibrational cooling.[11,56] The excited molecule undergoes intersystem crossing (ISC) to T_1 with a single-exponential time constant of $\tau_{ISC} = 102 \pm 5$ ps, resulting in the appearance of a series of triplet−triplet absorption bands that include a strong transition centered near 360 nm and several weaker transitions at longer wavelengths.[11,19,56]

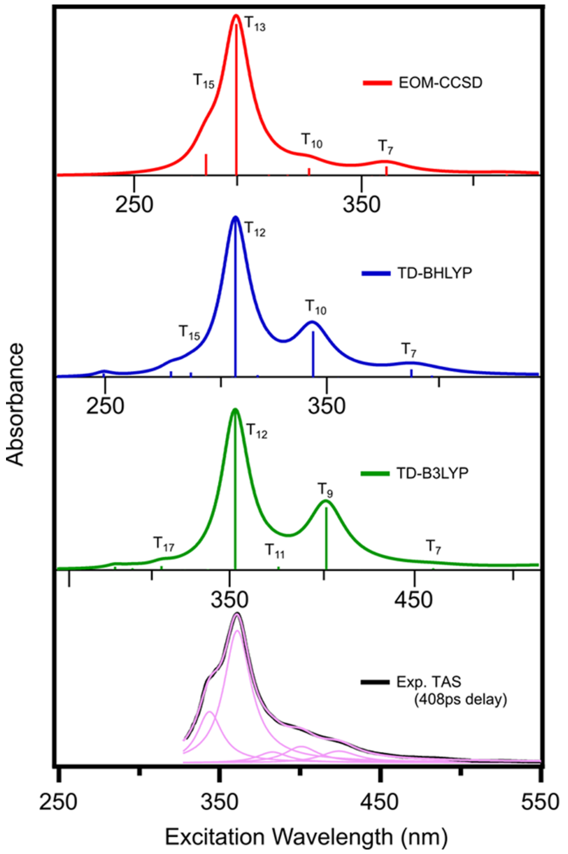

Figure 2. Electronic absorption spectra for the T_1 state of PT. Calculated spectra are offset by 0.720 (EOM-CCSD), 0.575 (TD-BHLYP), and 0.110 eV (TD-B3LYP) to align the strongest transition with experiments. Simulated spectra include 0.2 eV Lorentzian broadening. Pink lines show a deconvolution of the experimental spectrum with five Lorentzian bands.

Figure 2 compares the experimental absorption spectrum of T_1 at a time delay of 408 ps ($4 \times \tau_{ISC}$), with the calculated spectra of the triplet state from EOM-CCSD, TD-B3LYP, and TD-BHLYP. The figure includes a deconvolution of the experimental triplet absorption spectrum with a sum of five Lorentzian bands. The deconvolution uses the same adjustable bandwidth for all of the transitions. The best fit to the data gives a bandwidth of 0.197 ± 0.001 eV, with relatively small uncertainties in the band positions and amplitudes. Details of the deconvolution are given in Figure S3.

For comparison, the simulated spectra in Figure 2 have been shifted to align the strongest calculated transitions in each case with the maximum of the TA spectrum. The simulated spectra include Lorentzian broadening with FWHM of 0.2 eV, consistent with the deconvolution of the experimental spectrum. The three computational methods give slightly different $T_N \leftarrow T_1$ excitation energies, but the qualitative structures of all three calculated spectra are in good agreement with experiments. Each of the calculated spectra has a single, strong transition to T_{12} or T_{13}, depending on the method, as well as several weaker transitions. Although TD-B3LYP requires the smallest shift to align the strongest transition with experiments, the other methods reproduce the shape better, particularly EOM-CCSD. The calculations indicate that there are as many as six optically accessible states within ~0.4 eV of the state with the strongest transition.

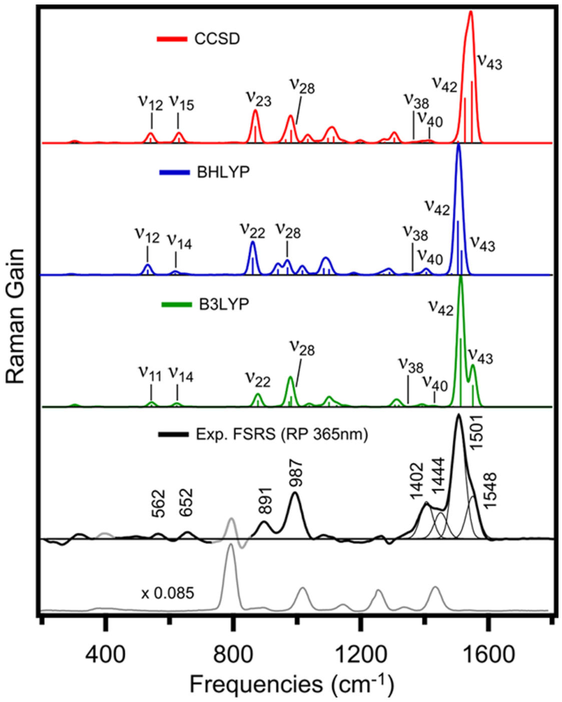

Figure 3. Raman spectra for the T_1 state of PT. Calculated off-resonance Raman spectra include 25 cm^{-1} Gaussian broadening and frequency correction factors given in the text. The experimental spectrum was measured with 365 nm Raman excitation and 408 ps delay, with thin black lines showing a deconvolution of the 1350−1600 cm^{-1} region using four Gaussian functions. The cyclohexane solvent spectrum (gray) is included for comparison.

4.2. Vibrational Assignments for the T_1 FSRS Spectrum.

The experimental FSRS spectrum for the T_1 state of PT is shown in Figure 3, along with the calculated off-resonance Raman spectra using B3LYP, BHLYP, and CCSD. A complete list of calculated frequencies and Raman activities is included in Table S2. The frequencies of the calculated spectra in Figure 3 are multiplied by empirical scaling factors of 0.970,[57] 0.924,[58] and 0.963[57] for B3LYP, BHLYP, and CCSD, respectively. The experimental spectrum was measured with the Raman pump excitation at 365 nm and a delay of 408 ps. The long time delay and resonance with the triplet absorption band ensure that the resonance-enhanced FSRS spectrum includes contributions from only the T_1 state.

Using the calculated frequencies as a foundation, we assign the Raman bands by identifying the vibrations most likely to have strong resonance enhancement.[19] We predict the resonance enhancements of the vibrational modes based on two criteria: (1) the mode must be totally symmetric (a′) to provide a nonzero contribution to the resonance Raman activity[17,28] and (2) the PES of the resonant electronic state

Table 1. Assignment of T_1 Raman Transitions

vibration	symmetry	calc. frequency[a] (cm^{-1})	calc. relative Raman intensity[b]	exp. frequency (cm^{-1})	exp. relative Raman intensity[b]	motion
ν_{11}	a'	544	0.035	562	0.030	C−S−C bend and phenyl dist.
ν_{14}	a'	622	0.027	652	0.071	C−S−C str. and phenyl dist.
ν_{22}	a'	877	0.096	891	0.146	C−C−C bend/ring dist.
ν_{28}	a'	981	0.234	987	0.396	C−C−C bend/phenyl dist.
ν_{38}	a'	1370	0.005	1402	0.295[c]	bridging C=C str. and C−H bend
ν_{39}	a'	1392	0.019			bridging C=C str. and C−H bend
ν_{40}	a'	1427	0.007	1444	0.208[c]	thienyl C=C str. and C−H bend
ν_{42}	a'	1513	1.000	1501	1.000[c]	C=C str. and phenyl dist.
ν_{43}	a'	1551	0.322	1548	0.339[c]	C=C str. and ring dist.

[a] B3LYP, includes frequency scaling factor of 0.970.[57] See Table S3 for assignments using BHLYP and CCSD. [b] Ratios of integrated band intensities relative to the band at 1513 (calc.) or 1501 cm^{-1} (exp.). The experimental Raman excitation wavelength is 365 nm. [c] From deconvolution of the 1350−1600 cm^{-1} region of the FSRS spectrum.

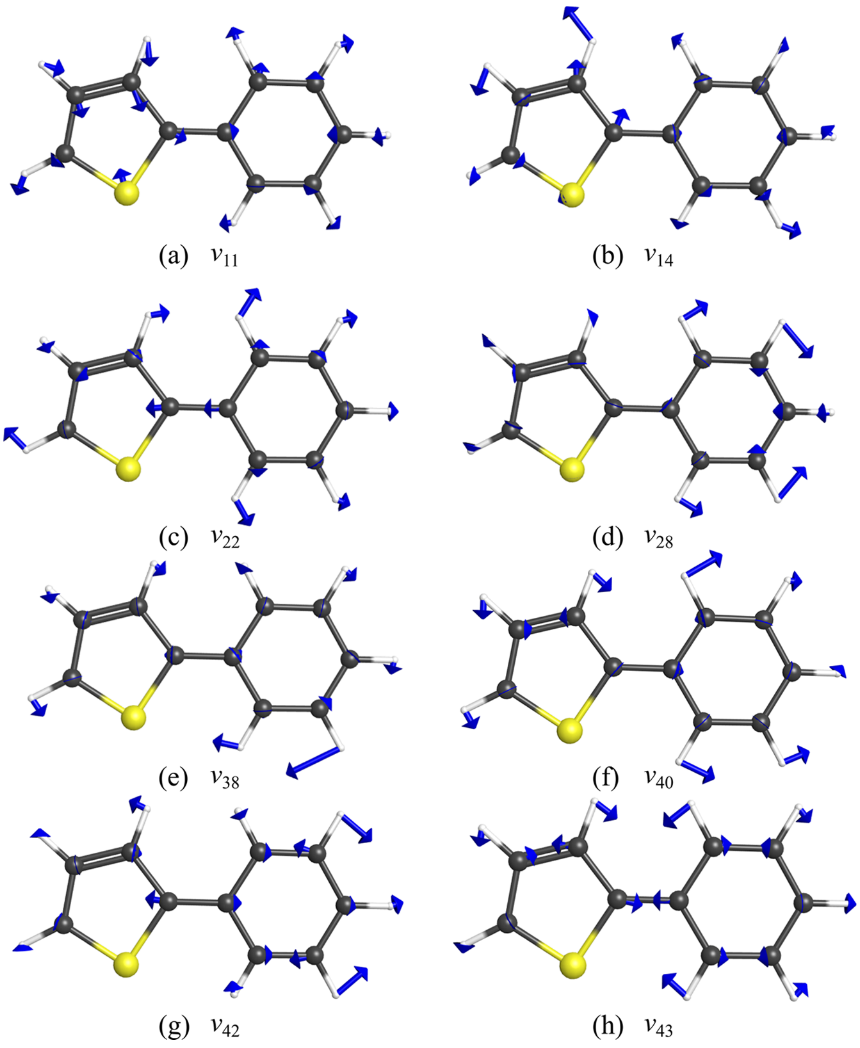
(a) ν_{11} (b) ν_{14}
(c) ν_{22} (d) ν_{28}
(e) ν_{38} (f) ν_{40}
(g) ν_{42} (h) ν_{43}

Figure 4. Vibrational displacement vectors for assigned vibrations of the T_1 state of PT (B3LYP).

will have a large gradient along the vibrational displacement coordinate of the T_1 normal mode.[6,7,31,38] We expect that the $T_N \leftarrow T_1$ transitions are most likely π−π^* excitations, and therefore, the largest gradients in T_N will be along vibrational modes with significant distortion of the π-conjugated framework of the molecule.[19,23]

The vibrational assignments based on B3LYP are listed in Table 1, and the nuclear displacement vectors for the assigned vibrations are represented in Figure 4. The majority of assignments are straightforward, as there is only one calculated totally symmetric vibration within ∼40 cm^{-1} of the experimental bands. Two noteworthy exceptions are the bands at 1402 and 1444 cm^{-1}, for which there are three possible assignments: ν_{38}, ν_{39}, and ν_{40}. While the FSRS signals may be attributed to any combination of these C=C stretching and C−H bending vibrations, our calculations of the resonance-enhanced Raman spectra (presented in a later section) predict ν_{38} and ν_{40} to have the strongest resonance enhancements despite their small amplitudes in the off-resonance spectra. Similarly, the band at 987 cm^{-1} could be assigned as either ν_{27} or ν_{28}, but the calculations are most consistent with the latter. The results for BHLYP and CCSD are similar to those for B3LYP, and the assignments for all three methods are listed in Table S3.

For a more quantitative comparison, Table 1 shows the relative intensities of the assigned Raman bands in the experimental and calculated (B3LYP) spectra. The ratios for the calculated intensities are relative to the strongest transition at 1513 cm^{-1}. The relative experimental intensities are obtained by integrating each Raman band and taking the ratio relative to the strongest band at 1501 cm^{-1}. To deconvolute the overlapping high-frequency Raman bands in the experimental FSRS spectrum, we fit the 1350−1600 cm^{-1} region of the spectrum to a sum of four Gaussian functions. We use a single, adjustable FWHM parameter of 46 cm^{-1} to match the experimental line width based on the instrument resolution. The deconvolution, shown in Figure 3, reveals at least four bands, including a band at 1548 cm^{-1} that appears as a shoulder of the stronger 1501 cm^{-1} band, and the two bands at 1402 and 1444 cm^{-1}, respectively. See Figure S4 for a more detailed description of the deconvolution.

Comparing the spectra in Figure 3 and the relative intensities in Table 1, we find good agreement between experiment and theory for most of the assigned vibrations. The relative intensities of the experimental bands agree with the calculations to within 10%, except for the bands at 1402 and 1444 cm^{-1}, which are significantly stronger in the experiment. The other computational methods have similar agreement to the experimental FSRS spectrum and relative intensities that differ from B3LYP by less than 20% in most cases (Table S3). Therefore, all of the simulated off-resonance spectra are in good agreement with the experimental FSRS spectrum, other than the 1402 and 1444 cm^{-1} bands, with B3LYP performing slightly better than the other methods. Good agreement between off-resonance calculations and the resonance-enhanced Raman spectra also has been reported in the literature for the triplet states of a number of other molecules.[25,26,59,60] In contrast, our previous studies of the excited singlet (S_1) states of PT, DPT, and other aryl-thiophenes showed significant disagreement in the intensities between the resonance-enhanced FSRS spectra and the calculated off-resonant S_1 Raman spectra.[19,23] To the best of our knowledge, the reason for the much weaker mode dependence of the resonance Raman enhancement for the triplet spectra compared with singlet spectra has not been addressed.

4.3. Wavelength Dependence of the T_1 FSRS Spectrum.

In order to explore resonance-enhancement effects in the T_1 spectrum of PT, we measure the Raman excitation wavelength dependence by tuning the Raman pump from the maximum absorption at 360 nm to a weaker band in the triplet absorption spectrum at 400 nm in ~5 nm increments (see green arrows in Figure 1). The FSRS signal is too weak to observe at longer wavelengths. Figure 5 shows the FSRS spectrum at each Raman excitation wavelength. To account for differences in the signal strength due to slight variation of the Raman pump power and beam overlap at the different pump wavelengths, we normalize the transient spectra based on the intensities of the solvent Raman bands at the different excitation wavelengths (Figure S2). We use the integrated intensities of the four dominant Raman bands of the pure solvent (801, 1028, 1266, and 1444 cm^{-1} of cyclohexane) to normalize the spectrum at each excitation wavelength. We also account for the $\omega_p(\omega_p - \omega_k)^3$ frequency dependence of the solvent Raman signal (eq 1) by multiplying each of the normalized spectra with an additional correction factor relative to the value at 400 nm.

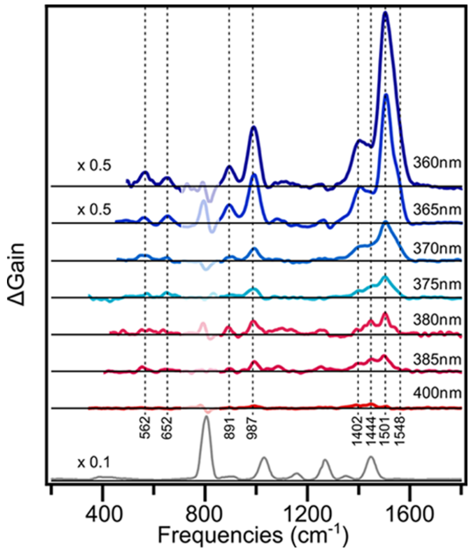

Figure 5. Excitation wavelength dependence of the FSRS spectrum for the T_1 state of PT. Vertical dashed lines indicate assigned vibrations from Table 1. The cyclohexane solvent spectrum (gray) is shown for comparison.

The Raman intensities of PT become significantly weaker as the excitation wavelength moves off resonance with the strongest $T_N \leftarrow T_1$ transition at 360 nm (Figure 5). Even at longer wavelengths, all of the bands assigned in Figure 3 are resolved, except the 652 and 1548 cm^{-1} bands, which fall below the noise level. We also observe a change in the relative intensities of the high-frequency bands. The 1501 cm^{-1} band, which dominates the spectrum at Raman pump wavelengths of ≤375 nm, becomes weaker in intensity than the 1402 and 1444 cm^{-1} bands at 400 nm excitation.

Figure 6 compares the Raman excitation profiles for each of the assigned vibrational bands with the profile of the triplet absorption spectrum. The intensities of the 1402, 1444, 1501, and 1548 cm^{-1} bands are obtained through the same deconvolution procedure at each wavelength, as described above for the FSRS spectrum at 365 nm. The deconvolution at each wavelength is shown in Figure S5. The relative behaviors of the mode-specific excitation profiles at longer wavelengths are difficult to distinguish in Figure 6a due to the strong resonance enhancement; therefore, we scale the excitation profiles by dividing the Raman gain at each excitation wavelength by the square of the triplet absorption signal $(\Delta A)^2$ at that wavelength in Figure 6b. The result is similar to dividing the Raman gain by a factor $|\mu_{NI}|^4$ in order to eliminate the mode-independent electronic contribution to the resonance enhancement (see below). Although the $(\Delta A)^2$ term is phenomenological, dividing by this value allows for a better comparison of the relative wavelength dependence of the

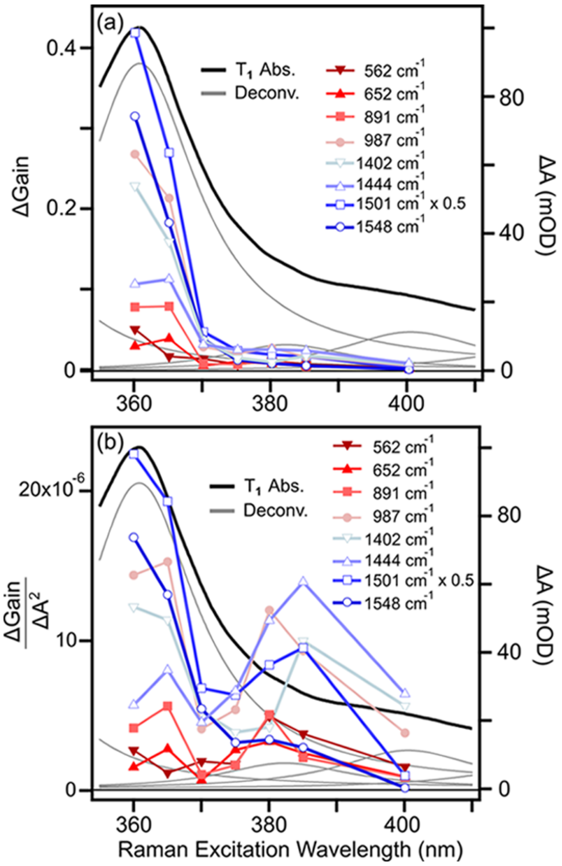

Figure 6. Raman excitation profiles for the assigned FSRS bands. (a) Comparison of resonance Raman intensities with the triplet absorption spectrum. (b) Comparison of resonance Raman intensities divided by the square of the triplet absorption $(\Delta A)^2$ at each wavelength to compensate for the strong electronic contribution to the resonance enhancement. The Lorentzian deconvolution of the T1 absorption spectrum from Figure 2 is shown as thin gray lines for comparison.

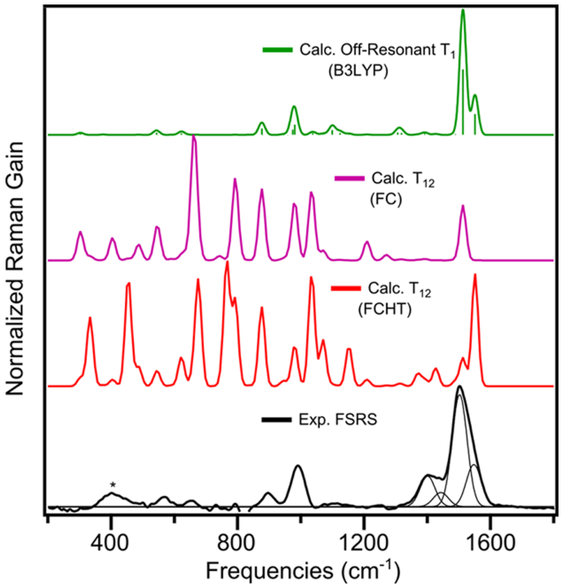

Figure 7. Comparison of simulated resonance Raman spectra from FC and FCHT approaches with calculated off-resonance and experimental FSRS spectra. FC/FCHT spectra are calculated for resonance with the T_{12} state at the adiabatic transition energy (26470 cm^{-1}). All simulated spectra are from B3LYP and include 0.970 frequency scaling factor and 25 cm^{-1} Gaussian broadening. Asterisk denotes an artifact from the CaF_2 sample window.

Raman gain profiles for the individual Raman bands by compensating for the strong electronic resonance enhancement of the experimental FSRS signal.

Figure 6b shows that the excitation profile of the 1548 cm^{-1} band closely follows the shape of the deconvoluted absorption band at 360 nm, whereas the profile of the 1444 cm^{-1} band has a maximum near 385 nm that roughly matches the center wavelength of a second transition in the deconvolution of the TA spectrum. The 987, 1402, and 1501 cm^{-1} bands have excitation profiles that follow both electronic transitions, initially dropping in intensity from 360 to 370 nm, increasing at 380−385 nm, and then decreasing again at longer wavelengths. In contrast, the 562, 652, and 891 cm^{-1} bands have comparatively little variation in normalized intensity with the Raman excitation wavelength. In order to explore the resonant $T_N \leftarrow T_1$ transitions that contribute to these mode-specific enhancement trends, we simulate the excited-state resonance Raman spectrum in the next section.

4.4. Simulated Resonance Raman Spectra. First, we simulate the resonance Raman spectrum of the triplet state of PT using the FC and FCHT methods with TD-B3LYP. The calculated spectra are shown in Figure 7 for resonance with a single electronic state at the adiabatic transition energy. It is immediately apparent that the calculations do not accurately reproduce the experimental spectrum, regardless of the inclusion of vibronic coupling. Both the FC and FCHT results are dominated by several strong bands below 1000 cm^{-1}, which contrasts with the experimental FSRS spectrum in the bottom panel of the figure.

Next, we simulate the resonance Raman spectrum using the gradient approximation[28,34,38] with TD-BHLYP, TD-B3LYP, and EOM-CCSD, as shown in Figure 8. The calculated Raman intensities have a strong dependence on the electronic absorption strength that makes it difficult to distinguish qualitative features for the weaker $T_N \leftarrow T_1$ transitions. Thus, the simulated resonance Raman spectra in Figure 8 are divided by the square of the electronic oscillator strength f^2, which is proportional to $|\mu_{NI}|^4$ for each transition. This scaling is similar in approach to the phenomenological scaling of the experimental Raman gain profiles in Figure 6b and reveals the gradients of each excited state T_N along the totally symmetric (a_1) normal modes of T_1. The figure only shows simulated spectra for the two states with the strongest electronic transitions at each level of theory. Gradient calculations for additional electronic states T_N are shown in Figure S6. Due to computational cost, we restrict the EOM-CCSD gradient calculations to include only the vibrations within a limited range of frequencies near the assigned experimental bands.

The simulated resonance Raman spectra from the gradient method have several features that are in good agreement with experiments. For example, many of the vibrations that have intensity in the simulated spectra match the assigned vibrations in Figure 3, including the 1501 and 1548 cm^{-1} bands. Notably, the Raman spectra for resonance with the strongest (T_{12} or T_{13}) and second strongest (T_9 or T_{10}) electronic transitions at each level of theory predict significant intensities in ν_{38} and ν_{40}, respectively. The resonance enhancements of ν_{38} and ν_{40} are consistent with the relatively strong experimental FSRS bands

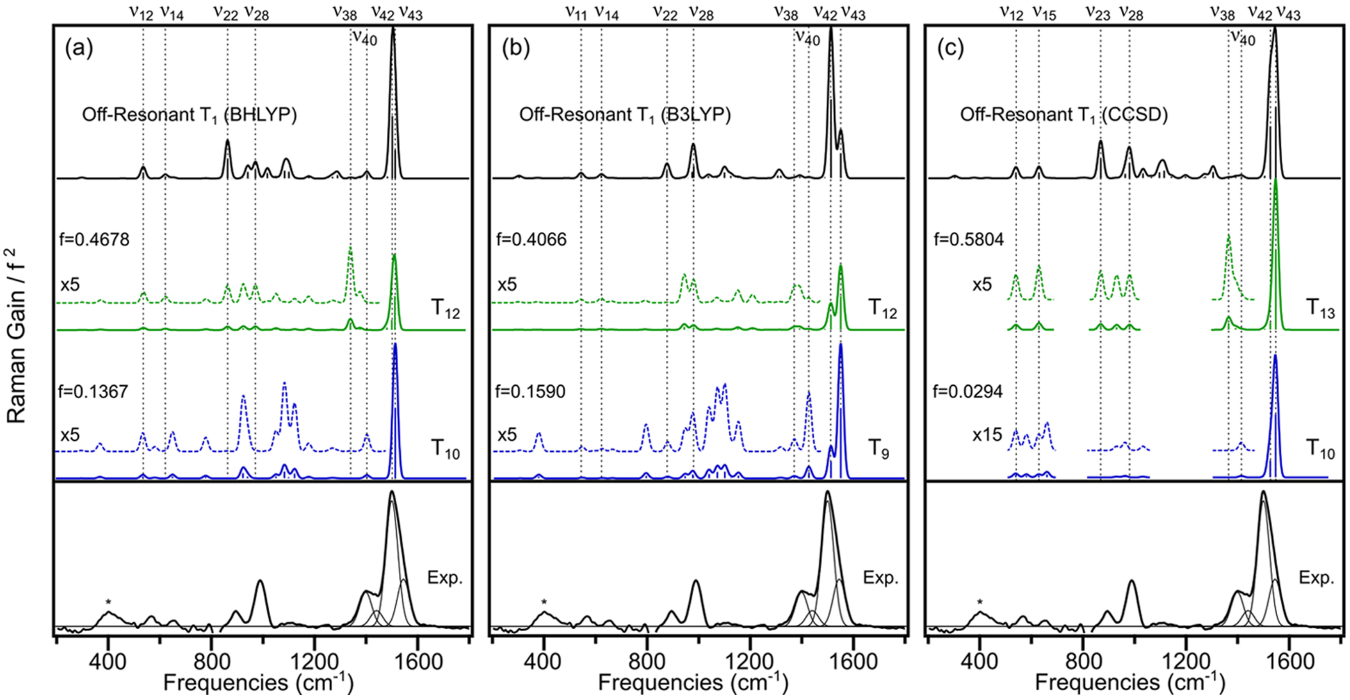

Figure 8. Comparison of simulated resonance Raman spectra from the gradient approximation with calculated off-resonance and experimental FSRS spectra: (a) TD-BHLYP; (b) TD-B3LYP; (c) EOM-CCSD. Simulated spectra are shown for resonance with the two strongest electronic transitions only and include frequency scaling and 25 cm^{-1} Gaussian broadening. Asterisk denotes an artifact from the CaF$_2$ sample window.

at 1402 and 1444 cm^{-1}. Furthermore, the stronger enhancement of ν_{40} for resonance with T$_9$/T$_{10}$ compared with T$_{12}$/T$_{13}$ matches the experimental excitation profile for the 1444 cm^{-1} band in Figure 6. We also point out that the Raman intensities of the low-frequency vibrations using the gradient method are much more reasonable than those from the FC/FCHT methods in Figure 7.

However, there are also some important discrepancies using the gradient approach that require closer investigation, such as the relative intensities of the 1501 and 1548 cm^{-1} Raman bands. The gradient calculations consistently predict stronger enhancement of the 1548 cm^{-1} band, in contrast with the dominant 1501 cm^{-1} band in both the experimental FSRS and calculated off-resonance spectra. To highlight this point, Figure 9 compares the high-frequency region of the experimental and simulated resonance Raman spectra. The figure shows the FSRS spectrum measured at 360 nm and includes only the calculated resonance Raman spectrum for the electronic state with the strongest transition strength (T$_{12}$ or T$_{13}$) in each computational method. The simulations also predict the wrong relative intensities of these high-frequency modes for resonance with the second strongest transition (T$_9$ or T$_{10}$, depending on the level of theory). The enhancement of the higher-frequency mode for both electronic states contrasts the experimental excitation profile, which decreases sharply with increasing wavelength for the 1548 cm^{-1} band. Similarly, the simulated resonance Raman spectra for T$_9$/T$_{10}$ have much lower intensities in the 987, 1402, and 1501 cm^{-1} bands compared with T$_{12}$/T$_{13}$, which does not match the recurrence of the experimental excitation profiles around 380−385 nm.

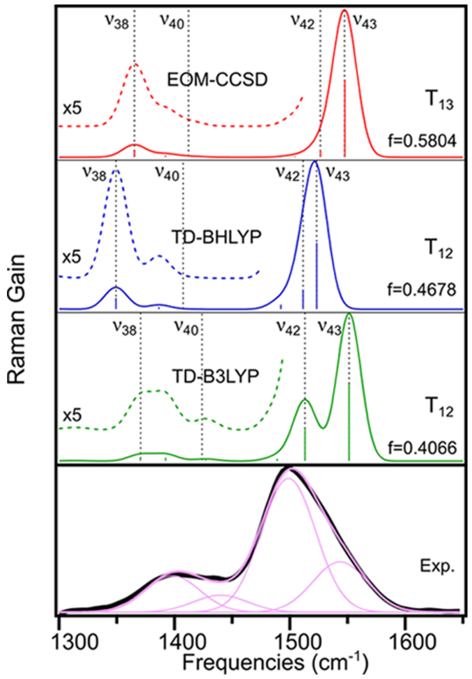

Figure 9. High-frequency region of the simulated resonance Raman spectra for the strongest T$_N$ ← T$_1$ transitions. Assigned vibrations are indicated by vertical dotted lines. Simulated Raman spectra are normalized and include 25 cm^{-1} Gaussian broadening. The experimental FSRS spectrum at the 360 nm Raman pump is shown for comparison, including deconvolution with four Gaussian bands.

5. DISCUSSION

The simulated Raman spectra using resonance and off-resonance methods agree with different aspects of the experimental FSRS spectrum of the T$_1$ state of PT, but neither approach fully reproduces the experimental results. Off-resonance calculations generally are in good agreement with the experimental spectrum, with a few notable exceptions where the calculations underestimate the intensities of the

DOI: 10.1021/acs.jpca.9b05955
J. Phys. Chem. A 2019, 123, 7720−7732

experimental bands. Simulated resonance Raman spectra using the FC/FCHT methods and the gradient approximation introduce the effects of electronic resonance but do not provide a better overall agreement with the experimental spectrum than the off-resonance calculations. The failure of the FC/FCHT methods in reproducing the experiment is likely a consequence of using the harmonic approximation to extrapolate the PES of the higher-lying triplet state from its minimum to the Franck−Condon geometry. On the other hand, simulated resonance Raman spectra using the gradient approximation correctly predict strong enhancements for several of the high-frequency vibrations (>1200 cm^{-1}) and explain the strong 1402 and 1444 cm^{-1} bands that are absent from the off-resonant spectra. However, the gradient approach does not accurately predict the relative intensities for many of the bands in the FSRS spectrum, for example, the bands at 1501 and 1548 cm^{-1}, or give the correct excitation profiles for many of the assigned vibrations.

In the limit of energetically well-separated electronic transitions, resonance Raman spectra are dominated by contributions from a single electronic state, as observed in our previous work on the resonance Raman spectrum for the S_1 state of DPT.[23] The experimental FSRS spectrum of DPT has strongly mode-dependent resonance enhancements and excitation profiles that follow the amplitude of the excited-state absorption spectrum. However, considering that the approach of calculating resonance enhancements for individual excited states is not sufficient to reproduce the observed spectra for the T_1 state of PT, we speculate that, in this case, it is necessary to consider the combined effect of multiple states simultaneously. This hypothesis is consistent with the deconvolution of the experimental TA spectrum in Figure 2, which shows multiple overlapping electronic transitions. The simultaneous signal enhancement from multiple states can be described in terms of additive and nonadditive effects. The gradient approximation should be able to capture the former by summing the properly weighted contributions from each adiabatic state T_N but not the latter without including nonadiabatic (i.e., HT) coupling. In principle, the FCHT method should be able to partially capture both effects, but the reliance on the harmonic approximation severely limits the applicability of that approach in this case because the harmonic potentials do not accurately represent the interacting electronic states far from their equilibrium geometries.

The role of multiple electronic states in the T_1 spectrum of PT is supported by the mode-specific experimental excitation profiles in Figure 6b. The Raman bands with vibrational frequencies above ∼900 cm^{-1} have the greatest intensity for either ∼360 or ∼380 nm excitation, suggesting resonance enhancement from at least two separate electronic transitions. The lower intensities for these vibrations near 370−375 nm may indicate a possible resonance de-enhancement due to nonadiabatic coupling between electronic states. As detailed in the literature,[61−63] resonance de-enhancement is a result of population transfer between coupled electronic states and would manifest as a decrease in the Raman excitation profile near the energy of the nonadiabatic curve crossing. Nonadiabatic effects are likely for the triplet states of PT, given the close proximity of several electronic transitions in both the calculated and experimental absorption spectra. However, our simulations do not account for these nonadditive de-enhancement effects.

Notably, the resonance Raman calculations using the gradient approximation correctly predict the strong resonance enhancements of the 1402 and 1444 cm^{-1} bands based on specific electronic resonances (T_{12}/T_{13} and T_9/T_{10}, respectively). Although these modes are very weak in the off-resonance calculation, the gradient calculations indicate strong enhancements of the two vibrations in resonance with the two different electronic states. The character of the vibrations may explain both the different intensities in the off-resonant and resonant spectra, as well as the different electronic states responsible for enhancement of the two modes. The displacements in Figure 4 show that modes ν_{38} and ν_{40} have more in-plane C−H bending than C=C stretching character. The C−H bending motion is not expected to significantly change the polarizability of the conjugated system, which would explain the relatively weak off-resonance intensities for these vibrations (cf. eq 4). In contrast, the calculated gradients along the normal mode coordinates for ν_{38} in T_{12}/T_{13} and for ν_{40} in T_9/T_{10} are larger than the gradients of most other vibrations, which explains the relatively large resonance Raman intensity of the experimental bands (eq 11). The different gradients for the two modes in the two electronic states may reflect the relative degree of delocalization of the C=C stretching excitation. Both vibrations have similar C−H bending character, but the C=C stretching is more localized on the thienyl ring for ν_{40}.

In contrast with the excitation profiles of the higher-frequency vibrations, the bands at 562, 652, and 891 cm^{-1} are relatively insensitive to the Raman excitation wavelength. The weak mode-specific enhancements of these FSRS bands may be a result of nonadditive homogeneous broadening effects and the overlapping contributions from several electronic transitions. Homogeneous broadening is likely to play a more significant role for low-frequency vibrations where the vibrational period is comparable to the dephasing time.[64−66] Homogeneous broadening is related to the phenomenological damping term $i\Gamma_n$ in the denominator of eq 2, which represents the dephasing of each vibronic state $|n\rangle$. Typical homogeneous broadening for vibronic transitions of a molecule in the condensed phase is of the order 10^1−10^2 cm^{-1}.[17,38,66] Thus, the denominator $\omega_{ni} - \omega_p - i\Gamma_n$ for each term in the sum-over-states expression of the transition polarizability (eq 2) is of the order 10^4 cm^{-1} for off-resonance transitions ($\omega_{ni} \approx 10^4$, $\omega_p = 0$) or 10^1−10^2 cm^{-1} for resonance terms ($\omega_{ni} - \omega_p \approx 0$) where the denominator is determined by the magnitude of Γ_n. As a result, the contributions to the transition polarizability for resonant electronic transitions are generally approximately 10^2−10^3 times larger than off-resonant transitions, which gives an enhancement of approximately 10^4−10^6 in the intensity (eq 1).

The FWHM broadening in the triplet spectrum of PT is 0.197 eV (or ∼1590 cm^{-1}). This is more than twice that of the relatively well isolated $S_N \leftarrow S_1$ absorption band of DPT (∼0.09 eV).[23] Thus, the deconvolution of the experimental TA spectrum of PT provides an upper limit for the magnitude of homogeneous broadening of ∼10^3 cm^{-1}. The additional broadening compared with a more typical Γ_n value of approximately 10^1−10^2 cm^{-1} reduces the maximum amplitude of the resonance enhancement for any individual electronic transition by 1−2 orders of magnitude and also spreads out the resonance across a wider range of excitation wavelengths. At the same time, the broadening of nearby transitions leads to contributions from those states as well. For example, the

B3LYP calculations predict transitions to T_{11} and T_{14} that are 0.24 eV below and 0.17 eV above the strongest transition to T_{12}, respectively. These differences in energy are comparable to the upper limit of Γ_n from the deconvolution of the experimental spectrum. Therefore, all three of these states could contribute to the Raman spectrum simultaneously.

Vibronic coupling may also play a role in determining the relative intensities in the resonance Raman spectrum of the T_1 state of PT. The off-resonance Raman spectra calculated with eq 3 already include contributions from B-term scattering because the polarizability derivative implicitly contains some vibronic coupling terms through the dipole derivative with respect to vibrational displacements, as described by Long.[17] Thus, the consistently good agreement between the off-resonance Raman spectra and the experiment could be an indication that vibronic coupling is involved. As mentioned above, the FC and FCHT calculations are not helpful in evaluating this effect due to shortcomings of the harmonic approximation, whereas the gradient approach neglects any explicit vibronic coupling contributions. Although beyond the scope of this work, it would be desirable to extend the gradient approximation to include such nonadditive, higher-order effects.

6. CONCLUSIONS

We report the excitation wavelength dependence of the FSRS spectrum for the T_1 state of PT and compare the trends we observe to simulated on- and off-resonance Raman spectra using several theoretical approaches. The experimental results provide a rigorous benchmark for the accuracy of the computational techniques, whereas the computational results highlight the difficulties of interpreting FSRS spectra involving more than one resonant or nearly resonant electronic transition. These results also point to important limitations of the FC and FCHT approaches for the calculation of resonance Raman spectra in the presence of broad, overlapping transitions. The more densely packed manifold of the high-lying electronic states makes it difficult to extrapolate the PES from the excited-state minimum to the Franck−Condon geometry using the harmonic approximation.

The mode-specific excitation profiles in the experimental FSRS spectrum may be explained by homogeneous broadening of the $T_N \leftarrow T_1$ transitions. A Lorentzian deconvolution of the triplet absorption spectrum indicates several overlapping transitions, each with significant homogeneous broadening. Estimates of an upper limit to the Γ_n values, based on the experimental TA spectrum, show that these values are roughly an order of magnitude larger than what is typically observed in resonance Raman measurements. The reasonably large Γ_n values increase the relative importance of the mode-specific resonance enhancement contributions from nearby transitions, which may explain the broad excitation profiles observed for the Raman bands. The significant homogeneous broadening is possibly a result of increased vibronic coupling between the electronic states of the triplet manifold. Thus, the good agreement between the off-resonance Raman calculations and the experimental spectrum may indicate that the contributions from multiple transitions and vibronic coupling effects have an influence on the FSRS spectrum that is comparable to or even larger than the electronic resonance condition. In summary, this work highlights the necessity of considering multiple contributions when extracting information about resonant electronic states in FSRS and helps explain the good agreement of off-resonant calculations with the resonance-enhanced FSRS spectra of the triplet states of PT.

■ ASSOCIATED CONTENT

Ⓢ Supporting Information

The Supporting Information is available free of charge on the ACS Publications website at DOI: 10.1021/acs.jpca.9b05955.

> Description of the FSRS baselining method, deconvolution of the experimental absorption and FSRS spectra, parameters from the calculations, and additional calculated resonance Raman spectra using the gradient method (PDF)

■ AUTHOR INFORMATION

Corresponding Authors

*E-mail: mcaricato@ku.edu (M.C.).
*E-mail: elles@ku.edu (C.G.E.).

ORCID
Marco Caricato: 0000-0001-7830-0562
Christopher G. Elles: 0000-0002-1408-8360

Notes

The authors declare no competing financial interest.

■ ACKNOWLEDGMENTS

The authors thank Kristen Burns for measuring the transient absorption spectrum of PT. This material is based upon work supported in part by the National Science Foundation through a Career Award (CHE-1151555) and the American Chemical Society Petroleum Research Fund (53045-DNI6), with additional support from the General Research Fund and startup funding from the University of Kansas.

■ REFERENCES

(1) McCamant, D. W.; Kukura, P.; Mathies, R. A. Femtosecond Time-Resolved Stimulated Raman Spectroscopy: Application to the Ultrafast Internal Conversion in *β*-Carotene. *J. Phys. Chem. A* **2003**, *107*, 8208−8214.

(2) Lee, S.-Y.; Zhang, D.; McCamant, D. W.; Kukura, P.; Mathies, R. A. Theory of Femtosecond Stimulated Raman Spectroscopy. *J. Chem. Phys.* **2004**, *121*, 3632−3642.

(3) Kukura, P.; McCamant, D. W.; Mathies, R. A. Femtosecond Stimulated Raman Spectroscopy. *Annu. Rev. Phys. Chem.* **2007**, *58*, 461−488.

(4) Dietze, D. R.; Mathies, R. A. Femtosecond Stimulated Raman Spectroscopy. *ChemPhysChem* **2016**, *17*, 1224−1251.

(5) Lee, S.-Y.; Heller, E. J. Time-Dependent Theory of Raman scattering. *J. Chem. Phys.* **1979**, *71*, 4777−4788.

(6) Shin, K. S. K.; Zink, J. I. Quantitative Evaluation of the Relationships Between Excitedstate Geometry and the Intensities of Fundamentals, Overtones, and Combination Bands in Resonance Raman Spectra. *Inorg. Chem.* **1989**, *28*, 4358−4366.

(7) Myers, A. B. 'Time-Dependent' Resonance Raman Theory. *J. Raman Spectrosc.* **1997**, *28*, 389−401.

(8) Pontecorvo, E.; Ferrante, C.; Elles, C. G.; Scopigno, T. Structural Rearrangement Accompanying the Ultrafast Electrocyclization Reaction of a Photochromic Molecular Switch. *J. Phys. Chem. B* **2014**, *118*, 6915−6921.

(9) Valley, D. T.; Hoffman, D. P.; Mathies, R. A. Reactive and Unreactive Pathways in a Photochemical Ring Opening Reaction from 2D Femtosecond Stimulated Raman. *Phys. Chem. Chem. Phys.* **2015**, *17*, 9231−9240.

(10) Batignani, G.; Pontecorvo, E.; Giovannetti, G.; Ferrante, C.; Fumero, G.; Scopigno, T. Electronic Resonances in Broadband Stimulated Raman Spectroscopy. *Sci. Rep.* **2016**, *6*, 18445.

(11) Batignani, G.; Pontecorvo, E.; Ferrante, C.; Aschi, M.; Elles, C. G.; Scopigno, T. Visualizing Excited-State Dynamics of a Diaryl Thiophene: Femtosecond Stimulated Raman Scattering as a Probe of Conjugated Molecules. *J. Phys. Chem. Lett.* **2016**, *7*, 2981−2988.

(12) Cen, Q.; He, Y.; Xu, M.; Wang, J.; Wang, Z. Wavelength Dependent Resonance Raman Band Intensity of Broadband Stimulated Raman Spectroscopy of Malachite Green in Ethanol. *J. Chem. Phys.* **2015**, *142*, 114201.

(13) Yu, W.; Donohoo-Vallett, P. J.; Zhou, J.; Bragg, A. E. Ultrafast Photo-Induced Nuclear Relaxation of a Conformationally Disordered Conjugated Polymer Probed with Transient Absorption and Femtosecond Stimulated Raman Spectroscopies. *J. Chem. Phys.* **2014**, *141*, No. 044201.

(14) Fujisawa, T.; Kuramochi, H.; Hosoi, H.; Takeuchi, S.; Tahara, T. Role of Coherent Low-Frequency Motion in Excited-State Proton Transfer of Green Fluorescent Protein Studied by Time-Resolved Impulsive Stimulated Raman Spectroscopy. *J. Am. Chem. Soc.* **2016**, *138*, 3942−3945.

(15) Weigel, A.; Dobryakov, A.; Klaumünzer, B.; Sajadi, M.; Saalfrank, P.; Ernsting, N. P. Femtosecond Stimulated Raman Spectroscopy of Flavin after Optical Excitation. *J. Phys. Chem. B* **2011**, *115*, 3656−3680.

(16) Myers Kelley, A. Resonance Raman and Resonance Hyper-Raman Intensities: Structure and Dynamics of Molecular Excited States in Solution. *J. Phys. Chem. A* **2008**, *112*, 11975−11991.

(17) Long, D. A. *The Raman Effect: A Unified Treatment of the Theory of Raman Scattering by Molecules*; Wiley: Chichester, New York, 2002.

(18) Neugebauer, J.; Reiher, M.; Kind, C.; Hess, B. A. Quantum Chemical Calculation of Vibrational Spectra of Large Molecules - Raman and IR Spectra for Buckminsterfullerene. *J. Comput. Chem.* **2002**, *23*, 895−910.

(19) Barclay, M. S.; Quincy, T. J.; Williams-Young, D. B.; Caricato, M.; Elles, C. G. Accurate Assignments of Excited-State Resonance Raman Spectra: A Benchmark Study Combining Experiment and Theory. *J. Phys. Chem. A* **2017**, *121*, 7937−7946.

(20) Tsumura, K.; Furuya, K.; Sakamoto, A.; Tasumi, M. Vibrational Analysis of transStilbene in the Excited Singlet State by Time-Dependent Density Functional Theory: Calculations of the Raman, Infrared, and Fluorescence Excitation Spectra. *J. Raman Spectrosc.* **2008**, *39*, 1584−1591.

(21) Dobryakov, A. L.; Ioffe, I.; Granovsky, A. A.; Ernsting, N. P.; Kovalenko, S. A. Femtosecond Raman Spectra of cis-Stilbene and trans-Stilbene with Isotopomers in Solution. *J. Chem. Phys.* **2012**, *137*, 244505−244516.

(22) Batignani, G.; Fumero, G.; Pontecorvo, E.; Ferrante, C.; Mukamel, S.; Scopigno, T. Genuine Dynamics vs Cross Phase Modulation Artifacts in Femtosecond Stimulated Raman Spectroscopy. *ACS Photonics* **2019**, *6*, 492−500.

(23) Quincy, T. J.; Barclay, M. S.; Caricato, M.; Elles, C. G. Probing Dynamics in Higher-Lying Electronic States with Resonance-Enhanced Femtosecond Stimulated Raman Spectroscopy. *J. Phys. Chem. A* **2018**, *122*, 8308−8319.

(24) ten Wolde, A.; Jacobs, H. J. C.; Langkilde, F. W.; Bajdor, K.; Wilbrandt, R.; Negri, F.; Zerbetto, F.; Orlandi, G. Triplet State Resonance Raman and Absorption Spectroscopy of a Configurationally Locked (Z)-Hexatriene: 1,2-Divinylcyclopentene. *J. Phys. Chem.* **1994**, *98*, 9437−9445.

(25) Zuo, P.; Ma, C.; Kwok, W. M.; Chan, W. S.; Phillips, D. L. Time-Resolved Resonance Raman and Density Functional Theory Study of the Deprotonation Reaction of the Triplet State of p-Hydroxyacetophenone in Water Solution. *J. Org. Chem.* **2005**, *70*, 8661−8675.

(26) Wang, C.; Angelella, M.; Doyle, S. J.; Lytwak, L. A.; Rossky, P. J.; Holliday, B. J.; Tauber, M. J. Resonance Raman Spectroscopy of the T1 Triplet Excited State of Oligothiophenes. *J. Phys. Chem. Lett.* **2015**, *6*, 3521−3527.

(27) Albrecht, A. C. On the Theory of Raman Intensities. *J. Chem. Phys.* **1961**, *34*, 1476−1484.

(28) Heller, E. J.; Sundberg, R.; Tannor, D. Simple Aspects of Raman scattering. *J. Phys. Chem.* **1982**, *86*, 1822−1833.

(29) Johnson, A. E.; Myers, A. B. Solvent Effects in the Raman Spectra of the Triiodide Ion: Observation of Dynamic Symmetry Breaking and Solvent Degrees of Freedom. *J. Phys. Chem.* **1996**, *100*, 7778−7788.

(30) Ma, H.; Liu, J.; Liang, W. Time-Dependent Approach to Resonance Raman Spectra Including Duschinsky Rotation and Herzberg−Teller Effects: Formalism and Its Realistic Applications. *J. Chem. Theory Comput.* **2012**, *8*, 4474−4482.

(31) Myers, A. B.; Mathies, R. A.; Tannor, D. J.; Heller, E. J. Excited State Geometry Changes from Preresonance Raman Intensities: Isoprene and Hexatriene. *J. Chem. Phys.* **1982**, *77*, 3857−3866.

(32) Dirac, P. A. M.; Fowler, R. H. The Quantum Theory of Dispersion. *Proc. R. Soc. A* **1927**, *114*, 710−728.

(33) Placzek, G. *Handbuch der Radiologie VI*; Marx, E., Ed.; Wiley-VCH Verlag GmbH & Co. KGaA: Weinheim, 1934, *2*, 290−374.

(34) Heller, E. J. Wavepacket Path Integral Formulation of Semiclassical Dynamics. *Chem. Phys. Lett.* **1975**, *34*, 321−325.

(35) Baiardi, A.; Bloino, J.; Barone, V. A General Time-Dependent Route to Resonance-Raman Spectroscopy including Franck-Condon, Herzberg-Teller and Duschinsky Effects. *J. Chem. Phys.* **2014**, *141*, 114108.

(36) Silverstein, D. W.; Jensen, L. Vibronic Coupling Simulations for Linear and Nonlinear Optical Processes: Simulation Results. *J. Chem. Phys.* **2012**, *136*, No. 064110.

(37) Baiardi, A.; Bloino, J.; Barone, V. Time-Dependent Formulation of Resonance Raman Optical Activity Spectroscopy. *J. Chem. Theory Comput.* **2018**, *14*, 6370−6390.

(38) Guthmuller, J. The Role of Herzberg-Teller Effects on the Resonance Raman Spectrum of trans-Porphycene Investigated by Time Dependent Density Functional Theory. *J. Chem. Phys.* **2018**, *148*, 124107.

(39) Pontecorvo, E.; Ferrante, C.; Elles, C. G.; Scopigno, T. Spectrally Tailored Narrowband Pulses for Femtosecond Stimulated Raman Spectroscopy in the Range 330-750 nm. *Opt. Express* **2013**, *21*, 6866−6872.

(40) Marangoni, M. A.; Brida, D.; Quintavalle, M.; Cirmi, G.; Pigozzo, F. M.; Manzoni, C.; Baronio, F.; Capobianco, A. D.; Cerullo, G. Narrow-Bandwidth Picosecond Pulses by Spectral Compression of Femtosecond Pulses in Second-order Nonlinear Crystals. *Opt. Express* **2007**, *15*, 8884−8891.

(41) Marangoni, M.; Brida, D.; Conforti, M.; Capobianco, A. D.; Manzoni, C.; Baronio, F.; Nalesso, G. F.; De Angelis, C.; Ramponi, R.; Cerullo, G. Synthesis of Picosecond Pulses by Spectral Compression and Shaping of Femtosecond Pulses in Engineered Quadratic Nonlinear Media. *Opt. Lett.* **2009**, *34*, 241−243.

(42) Lee, J.; Challa, J. R.; McCamant, D. W. Pump Power Dependence in Resonance Femtosecond Stimulated Raman Spectroscopy. *J. Raman Spectrosc.* **2013**, *44*, 1263−1272.

(43) Becke, A. D. A New Mixing of Hartree-Fock and Local Density-Functional Theories. *J. Chem. Phys.* **1993**, *98*, 1372−1377.

(44) Becke, A. D. Density-Functional Thermochemistry. III. The Role of Exact Exchange. *J. Chem. Phys.* **1993**, *98*, 5648−5652.

(45) Koch, H.; Jo/rgensen, P. Coupled Cluster Response Functions. *J. Chem. Phys.* **1990**, *93*, 3333−3344.

(46) Stanton, J. F.; Bartlett, R. J. The Equation of Motion Coupled-cluster Method. A Systematic Biorthogonal Approach to Molecular Excitation Energies, Transition Probabilities, and Excited State Properties. *J. Chem. Phys.* **1993**, *98*, 7029−7039.

(47) Koch, H.; Kobayashi, R.; Sanchez de Merás, A.; Jo/rgensen, P. Calculation of Size-Intensive Transition Moments from the Coupled Cluster Singles and Doubles Linear Response Function. *J. Chem. Phys.* **1994**, *100*, 4393−4400.

(48) Staniszewska, M.; Kupfer, S.; Łabuda, M.; Guthmuller, J. Theoretical Assessment of Excited State Gradients and Resonance Raman Intensities for the Azobenzene Molecule. *J. Chem. Theory Comput.* **2017**, *13*, 1263−1274.

DOI: 10.1021/acs.jpca.9b05955
J. Phys. Chem. A 2019, 123, 7720−7732

(49) Piontkowski, Z.; McCamant, D. W. Excited-State Planarization in Donor-Bridge Dye Sensitizers: Phenylene Versus Thiophene Bridges. *J. Am. Chem. Soc.* **2018**, *140*, 11046−11057.

(50) Dunning, T. H., Jr. Gaussian Basis Sets for Use in Correlated Molecular Calculations. I. The Atoms Boron Through Neon and Hydrogen. *J. Chem. Phys.* **1989**, *90*, 1007−1023.

(51) Čížek, J. *Advances in Chemical Physics*; John Wiley & Sons, Inc.: 2007; pp 35−89.

(52) Purvis, G. D., III; Bartlett, R. J. A Full Coupled-Cluster Singles and Doubles Model: The Inclusion of Disconnected Triples. *J. Chem. Phys.* **1982**, *76*, 1910−1918.

(53) Scuseria, G. E.; Janssen, C. L.; Schaefer, H. F., III An Efficient Reformulation of the closed-shell Coupled Cluster Single and Double Excitation (CCSD) Equations. *J. Chem. Phys.* **1988**, *89*, 7382−7387.

(54) Scuseria, G. E.; Schaefer, H. F., III Is Coupled Cluster Singles and Doubles (CCSD) More Computationally Intensive than Quadratic Configuration Interaction (QCISD)? *J. Chem. Phys.* **1989**, *90*, 3700−3703.

(55) Frisch, M. J.; Trucks, G. W.; Schlegel, H. B.; Scuseria, G. E.; Robb, M. A.; Cheeseman, J. R.; Scalmani, G.; Barone, V.; Mennucci, B.; Petersson, G. A. et al. *Gaussian09* Revision D.01, Gaussian Inc.: Wallingford CT, 2009.

(56) Zheldakov, I. L.; Wasylenko, J. M.; Elles, C. G. Excited-State Dynamics and Efficient Triplet Formation in Phenylthiophene Compounds. *Phys. Chem. Chem. Phys.* **2012**, *14*, 6211−6218.

(57) *NIST Computational Chemistry Comparison and Benchmark Database, NIST Standard Reference Database Number 101.* (accessed 20 June 2019); http://cccbdb.nist.gov/.

(58) Merrick, J. P.; Moran, D.; Radom, L. An Evaluation of Harmonic Vibrational Frequency Scale Factors. *J. Phys. Chem. A* **2007**, *111*, 11683−11700.

(59) Xue, J.; Vyas, S.; Du, Y.; Luk, H. L.; Chuang, Y. P.; But, T. Y. S.; Toy, P. H.; Wang, J.; Winter, A. H.; Phillips, D. L.; et al. Time-Resolved Resonance Raman and Computational Investigation of the Influence of 4-Acetamido and 4-N-Methylacetamido Substituents on the Chemistry of Phenylnitrene. *J. Phys. Chem. A* **2011**, *115*, 7521−7530.

(60) Langkilde, F. W.; Wilbrandt, R.; Brouwer, A. M.; Negri, F.; Zerbetto, F.; Orlandi, G. Molecular Structure of Stilbene in the T1 State. Transient Resonance Raman Spectra of Stilbene Isotopomers and Quantum Chemical Calculations. *J. Phys. Chem.* **1994**, *98*, 2254−2265.

(61) Heather, R.; Metiu, H. Time-Dependent Theory of Raman Scattering for Systems with Several Excited Electronic States: Application to a H_3^+ Model System. *J. Chem. Phys.* **1989**, *90*, 6903−6915.

(62) Reber, C.; Zink, J. I. Resonance Raman Deenhancement Caused by Excited-State Potential Surface Crossing. *J. Phys. Chem.* **1992**, *96*, 571−576.

(63) Wang, X.; Valverde-Aguilar, G.; Weaver, M. N.; Nelsen, S. F.; Zink, J. I. Resonance Raman De-enhancement Caused by Excited State Mixed Valence. *J. Phys. Chem. A* **2007**, *111*, 5441−5447.

(64) Myers, A. B.; Harris, R. A.; Mathies, R. A. Resonance Raman Excitation Profiles of Bacteriorhodopsin. *J. Chem. Phys.* **1983**, *79*, 603−613.

(65) Myers, A. B.; Trulson, M. O.; Mathies, R. A. Quantitation of Homogeneous and Inhomogeneous Broadening Mechanisms in trans-Stilbene Using Absolute Resonance Raman Intensities. *J. Chem. Phys.* **1985**, *83*, 5000−5006.

(66) Myers, A. B.; Trulson, M. O.; Pardoen, J. A.; Heeremans, C.; Lugtenburg, J.; Mathies, R. A. Absolute Resonance Raman Intensities Demonstrate that the Spectral Broadening induced by the β-Ionone Ring in Retinal is Homogeneous. *J. Chem. Phys.* **1986**, *84*, 633−640.